Volume 16
Number 46
14 December 2020
Pages 10389–10576

Soft Matter

rsc.li/soft-matter-journal

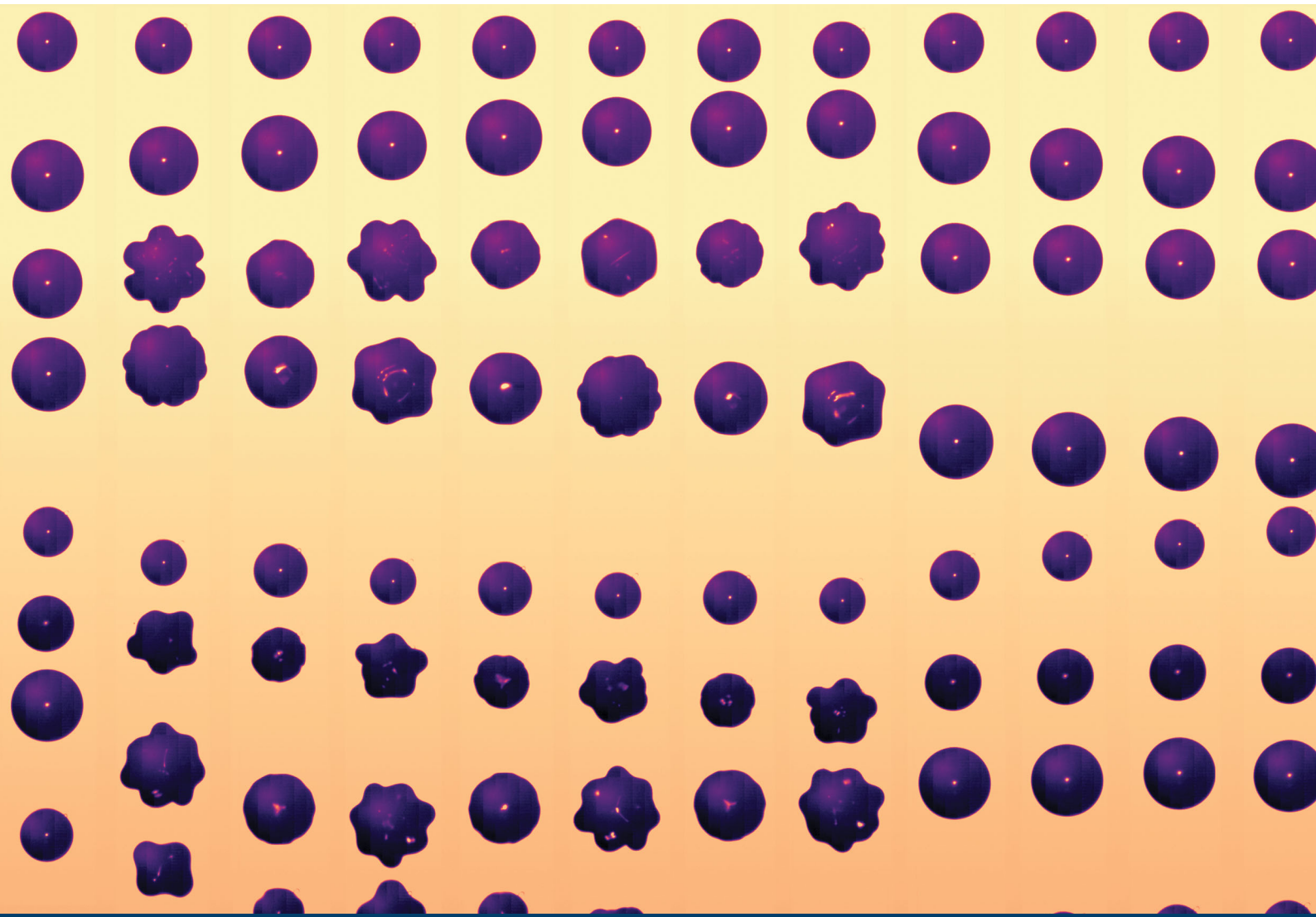

Soft Matter Lectureship winner 2020: Valeria Garbin

ISSN 1744-6848

ROYAL SOCIETY OF CHEMISTRY

PAPER
Brice Saint-Michel and Valeria Garbin
Acoustic bubble dynamics in a yield-stress fluid

Soft Matter

PAPER

View Article Online
View Journal | View Issue

Cite this: *Soft Matter*, 2020, **16**, 10405

Acoustic bubble dynamics in a yield-stress fluid†

Brice Saint-Michel ‡ and Valeria Garbin *‡

Yield-stress fluids naturally trap small bubbles when their buoyancy applies an insufficient stress to induce local yielding of the material. Under acoustic excitation, trapped bubbles can be driven into volumetric oscillations and apply an additional local strain and stress that can trigger yielding and assist their release. In this paper we explore different regimes of microbubble oscillation and translation driven by an ultrasound field in a model yield-stress fluid, a Carbopol microgel. We first analyse the linear bubble oscillation dynamics to measure the local, high-frequency viscosity of the material. We then use acoustic pressure gradients to induce bubble translation and examine the elastic part of the response of the material below yielding. We find that, at moderate pressure amplitude, the additional stresses applied by volumetric oscillations and acoustic radiation forces do not lead to any detectable irreversible bubble motion. At high pressure amplitude, we observe non-spherical shape oscillations that result in erratic bubble motion. The critical pressures we observe differ from the predictions of a recent model of shape oscillations in soft solids. Based on our findings, we discuss possible reasons for the lack of bubble release in Carbopol and suggest other systems in which ultrasound-assisted bubble rise may be observed.

Received 4th June 2020,
Accepted 30th September 2020

DOI: 10.1039/d0sm01044h

rsc.li/soft-matter-journal

1 Introduction

Yield-stress fluids encompass a wide range of materials including foams, suspensions, emulsions and microgels.[1,2] These materials exhibit a threshold in applied stress, called the yield stress, below which the material behaves like a solid, and above which it flows like a liquid. A clear manifestation of the yield stress is the presence of trapped bubbles, when their buoyancy force is too small to yield the material. Trapped bubbles can be beneficial, for instance when they are used to impart texture to a food product, or they can be detrimental as they can negatively affect the thermal conductivity or optical transparency of a material. Strategies to control the amount and size distribution of trapped bubbles are therefore important in processing of formulations and advanced materials. There is some experimental evidence that driving bubbles into volumetric oscillations in yield-stress fluids can assist their removal,[3] but the effect of oscillations on yielding is poorly understood. This lack of understanding is particularly detrimental to the development of controlled bubble removal methods.

Understanding bubble dynamics in yield-stress fluids is particularly challenging since their rheology is not even fully understood in the case of simple shear. Yield-stress fluids are only well-understood in the limit of very small shear stresses where a linear elastic behaviour is recovered, or for large, steady stresses for which their flow rheology usually obeys the Herschel–Bulkley equation.[1] For intermediate stresses, experimental results performed under steady or large amplitude oscillatory shear[4] have evidenced that yield-stress fluids exhibit non-linear,[5] time-dependent, cooperative[6] behaviour. Such features are only captured by the most recent microscopic[7] and continuum mechanics models.[8]

The capacity of a yield-stress fluid to entrap bubbles up to a critical effective radius R_c can be expressed as the dimensionless number $Y_c^{-1} = 2\rho_l g R_c/3\sigma_Y$, where ρ_l is the liquid density, g is the acceleration due to gravity and σ_Y is the yield stress of the material.[9] Even with the most conservative estimate, a yield stress of only 10 Pa causes trapping of bubbles up to $2R_c$ = 6 mm in diameter. Removing bubbles below the critical size can be achieved by centrifuging,[10] applying a vacuum, or by using low-frequency ($\sim$100 Hz) vibrations to suppress the yield stress in fragile granular networks.[11] These techniques alter the physical parameters at play in the definition of Y_c^{-1} rather than fundamentally altering this criterion.

Bubbles are however not passive under the application of vibrations and acoustic excitations, as the dynamic pressure field drives them into volumetric oscillations.[12] Oscillating bubbles apply a local strain field to the surrounding material, which in turn reacts by exerting a stress onto the bubble, altering the oscillation dynamics. Bubble dynamics in Newtonian liquids[12] and soft solids[13] is now a well-established topic,

Department of Chemical Engineering, Imperial College London, London SW7 2AZ, UK

† Electronic supplementary information (ESI) available. See DOI: 10.1039/d0sm01044h

‡ Present address: Department of Chemical Engineering, Delft University of Technology, Delft 2629 HZ, The Netherlands. E-mail: v.garbin@tudelft.nl

motivated *e.g.* by the direct role played by bubble collapse in therapeutic laser or ultrasound tissue ablation.[14,15] Bubble radius time profiles are now even used either in the linear regime[16] or the strongly non-linear, cavitation regime[17] to extract local rheological properties of soft solids.

In yield-stress fluids, oscillating bubbles may apply a strain that is sufficient to locally yield the material, defining a yielded, fluid region. Bubble rise may then proceed in this confined region even if their size is well below R_c. The size and shape of this region has a key influence on the bubble rising velocity, and ultimately in the efficiency of the removal process. While the shape of the yielded region has been investigated in great detail for passive bubble rise,[9,18] the case of oscillating bubbles has only been examined very recently.[19,20] Building upon the progress in modelling both bubble dynamics in soft materials[13] and the rheology of yield-stress fluids,[21] these articles confirm that bubble rise is indeed possible for bubbles below R_c;[19] they also compute the minimum oscillation amplitude required to initiate yielding.[20] To the best of our knowledge, these numerical and theoretical results have not yet been compared to experiments: experimental articles so far have focused on the case of bubble removal in a shear-thinning, viscoelastic surrounding fluid[22] and removal in yield-stress fluids for bubbles already close to the static rise radius at rest, R_c.[3]

In this article, we conduct experiments to test the criterion for medium yielding and bubble removal that we previously derived,[20] using a Carbopol microgel as a model yield-stress fluid. We investigate the oscillation dynamics of initially spherical bubbles (100–200 μm) excited by a standing-wave ultrasound field with controlled frequency (19–30 kHz), acoustic pressure amplitude, and spatial distribution of pressure gradients. We measure the resonance curve of the bubbles, their mobility in a pressure gradient and the onset of non-spherical shape oscillations. We extract the viscosity and linear elastic modulus of the material, and compare these measurements to the predictions of the model.[20] We finally conclude on the efficiency of bubble removal through bubble oscillation in yield-stress fluids.

2 Bubble dynamics in yield-stress fluids

2.1 Governing equations for bubble oscillations

We briefly recall here the physics of the linear oscillations of a spherical bubble in a yield-stress fluid we derived in a previous article.[20] We will show in Section 3.4 that the assumptions of spherical bubble and linear dynamics are reasonable given the size of the bubbles and the rheological properties of the fluid that we use in the experiments.

A bubble with equilibrium radius R_0 is driven into volumetric oscillations under an acoustic excitation at a frequency f, *i.e.* a sinusoidal applied pressure $p(t) = p\sin(2\pi ft)$ far away from the bubble. The time-dependent radius, $R(t)$, is:

$$R(t) = R_0[1 + \zeta(t)]. \quad (1)$$

Applying the momentum and the mass conservation for the fluid between the spherical bubble surface $r = R(t)$ and $r \to \infty$ yields a generalised Rayleigh–Plesset equation valid for arbitrary fluids.[23] Previously our group has derived a model for bubble dynamics in yield-stress fluids by combining the generalised Rayleigh–Plesset equation[23] with the elasto-visco-plastic rheological model proposed by Saramito.[21] The details of the full model can be found in ref. 20. We recall here that for small-amplitude oscillations and below the yield point, the rheological model reduces to a Kelvin–Voigt viscoelastic solid of linear elastic modulus G and solvent viscosity η_s. A Taylor expansion of the momentum balance valid at order 1 in ζ may then be derived following the classical linear theory of bubble dynamics:[24]

$$\ddot{\zeta} + 2\beta\dot{\zeta} + 4\pi^2 f_0^2\zeta = -\frac{p}{\rho R_0^2}\sin(2\pi ft), \quad (2)$$

in which ρ is the fluid density, assumed to be a constant, and β and f_0 are respectively the damping coefficient and the natural frequency of the bubble oscillations. These two quantities depend *a priori* on the rheology of the fluid.

Eqn (2) is a standard second-order linear differential equation that we can reformulate in the frequency domain. We then obtain the second-order transfer function for the bubble oscillation amplitude ζ in the spirit of earlier works on bubble spectroscopy:[16,25,26]

$$\zeta(t) = \zeta\sin(2\pi ft + \phi) \quad (3a)$$

$$\zeta = \frac{p/\rho R_0^2}{4\pi\sqrt{\pi^2(f_0^2 - f^2)^2 + \beta^2 f^2}} \quad (3b)$$

$$\phi = \frac{\pi}{2} + \arctan\left[\frac{\pi}{\beta f}\left(f_0^2 - f^2\right)\right] \quad (3c)$$

The amplitude part of the transfer function [eqn (3b)] gives the resonance curve of the bubble. The phase lag between the bubble oscillation and the pressure field ϕ made explicit in eqn (3c) spans from π for $f \ll f_0$ in the low frequency case to 0 for $f \gg f_0$ in the high frequency case.

The natural oscillation frequency f_0 based on the model of Saramito[21] is derived in ref. 20:

$$f_0^2 = \frac{3\kappa p_0 + 2(3\kappa - 1)\Gamma/R_0 + 4G}{4\pi^2\rho R_0^2}, \quad (4)$$

in which Γ is the surface tension between the gas and the fluid and p_0 is the ambient atmospheric pressure. We also introduce here the polytropic exponent $1.0 \le \kappa \le 1.4$ that indicates the nature of the thermodynamic process occurring in the bubble, from isothermal ($\kappa = 1$) to adiabatic ($\kappa = 1.4$) depending on the thermal Péclet number.[24]

For very soft materials for which $G \ll p_0$, and for sufficiently large bubbles, *i.e.* for $R_0 \gg \Gamma/p_0 = 1.0$ μm, we recover the

standard Minnaert frequency[27] for a given bubble radius R_0:

$$f_m = \frac{1}{2\pi R_0}\sqrt{\frac{3\kappa p_0}{\rho}}. \quad (5)$$

Eqn (5) may be used as well to derive a resonant radius R_m for a given oscillation frequency f. We also recall the predictions for the damping parameter β:[20,26]

$$\beta = \frac{2\eta_{eff}}{\rho {R_0}^2} = \frac{2}{\rho {R_0}^2}\left[\eta_s + \frac{\pi^2 \rho f^2 {R_0}^3}{c} + \frac{3p_0\kappa'}{8\pi f}\right] \quad (6)$$

The three terms at the right hand side of eqn (6) respectively account for viscous dissipation proportional to the solvent viscosity η_s in the Kelvin–Voigt model; acoustic scattering of the bubble, and thermal dissipation, in which the dimensionless quantity κ' is related to the polytropic exponent κ introduced earlier.[24] Appendix B shows the relative magnitude of each contribution to β for our experiments. The relative uncertainty on these quantities is discussed in ESI,† Section S1.

2.2 Acoustic radiation forces

Gradients in a pressure field exert a force $\mathbf{F} = -V\boldsymbol{\nabla}p$ on objects of volume V. In a standing wave field $p(\mathbf{x},t) = p(\mathbf{x})\sin(2\pi ft)$, the average force $\langle\mathbf{F}\rangle$ applied on an incompressible object of fixed volume V over one oscillation cycle is zero. Because bubbles expand and contract in response to oscillations in pressure, the same pressure gradient applies a larger net force on the object when its radius is large than when it is small. This leads to a net force over one oscillation period called Bjerknes force:[28]

$$\langle\mathbf{F}(\mathbf{x})\rangle = -2\pi {R_0}^3 \boldsymbol{\nabla}p(\mathbf{x})\zeta\cos(\phi). \quad (7)$$

For a driving frequency f and an equilibrium bubble size R_0, small bubbles for which $\cos(\phi) = -1$ will move towards high pressure areas (named anti-nodes) whereas large bubbles for which $\cos(\phi) = +1$ will move towards low pressure areas (nodes), a classical result in Newtonian fluids.[29] Bjerknes forces are non-linear as both $\boldsymbol{\nabla}p$ and ζ are proportional to the applied pressure. They are particularly efficient at pushing and pulling bubbles against gravity when the relative pressure gradient $|\boldsymbol{\nabla}p/p|$ is high.

Following eqn (3b) the pressure p required to obtain a constant oscillation amplitude ζ for all bubble radii R_0 is much higher far away from the resonance condition than at resonance. As a consequence, for an imposed oscillation amplitude ζ the pressure gradient $\boldsymbol{\nabla}p$ in eqn (7) and the Bjerknes forces will also be stronger away from resonance. We will use this strategy in Section 4.3 to apply strong Bjerknes forces while remaining in the linear range of the bubble oscillation amplitude ζ.

Recent articles have related the force applied to spherical objects and their displacement in purely elastic[30] or Kelvin–Voigt viscoelastic solids,[31] which can then be applied to yield-stress fluids for relatively small deformations. Assuming the pressure gradient $\boldsymbol{\nabla}p$ at location $\mathbf{x}$ is directed alongside z we have:

$$\frac{\Delta z(\mathbf{x})}{R_0} = \frac{1}{R_0}\left\langle\frac{F_z(\mathbf{x},t)}{4\pi G R(t)}\right\rangle = -\frac{1}{3}\frac{R_0}{G}\nabla_z p(x)\zeta\cos(\phi) \quad (8)$$

Eqn (8) remains valid as long as the oscillations do not alter the properties of the fluid. Interestingly, it provides a measurement of G that is unaffected by Γ and p_0 in contrast with eqn (4). We will use eqn (8) to measure G in Section 4.3.

2.3 Yielding criteria and impact on bubble dynamics

2.3.1 Yielding to oscillations. When no pressure gradient is present, the centre of the bubble is not moving and the strain field is spherically symmetric. Its expression in the spherical reference frame (r,θ,φ) centred on the bubble reads:[32]

$$\varepsilon_{rr}(r,t) = \left(1 + \frac{R(t)^3 - {R_0}^3}{r^3}\right)^{-4/3} - 1 \simeq -4\zeta(t)\frac{{R_0}^3}{r^3} \quad (9)$$

The Kelvin–Voigt model, assumed to be valid below yielding, expresses the applied stress as a sum of an elastic stress $G\boldsymbol{\varepsilon}$ and a viscous stress $\eta_s\dot{\boldsymbol{\varepsilon}}$. For sufficiently large oscillation amplitudes, the elastic stresses may satisfy the von Mises yield criterion[20,33] in a corona of fluid surrounding the bubble. The material then follows a Kelvin–Voigt rheology only outside of the yielded region, including at its edge, located at a distance r_Y from the centre of the bubble:

$$\left(\frac{r_Y}{R_0}\right)^3 = \frac{2\sqrt{3}G}{\sigma_Y}|\zeta(t)| \quad (10)$$

Eqn (10) defines the extent r_Y of the yielded region as a function of time. Fluid yielding starts when the yielded region exceeds the bubble size at rest R_0 at least once during an oscillation cycle. This simplified yielding criterion reads $\zeta \geq \zeta_c = \sigma_Y/2\sqrt{3}G$ and we hypothesise it is a necessary condition to initiate irreversible bubble rise.

In the yielded region, the purely elastic component of the Kelvin–Voigt model becomes a Maxwell element,[21] keeping its elastic modulus G and adding a non-linear plastic degree of deformation of viscosity η_{evp}, traditionally defined as $K\dot{\varepsilon}^{n-1}$ in rotational rheology. The elasto-plastic crossover time of the yielded material is $(K/G)^{1/n}$: the yielded material remains predominantly elastic below this time scale while plastic deformation dominates above it. Bubble oscillation dynamics is then only affected by yielding when the applied frequency satisfies $2\pi f(K/G)^{1/n} \leq 1$, in agreement with numerical simulations.[20]

Bubbles also apply a constant stress onto the fluid due to buoyancy or acoustic radiation forces. Hence, these forces will act on the yielded material during the whole time N/f of the acoustic excitation. Irreversible bubble displacement may then be observed provided that $f/N(K/G)^{1/n} \leq 1$.

2.3.2 Yielding to acoustic radiation forces. A second bubble release criterion can be computed from acoustic radiation forces, ignoring the contribution of the oscillatory stresses. We can compare the average acoustic radiation stress

$\sigma_{ac} = \langle F_z/2\pi R^2 \rangle$ to the yield-stress in direct analogy with the yielding parameter Y_c^{-1} used for gravity-driven bubble rise. This critical parameter varies between 1.1 for the most efficient, inverted teardrop shapes[34] to 5.1 for bubbles that are almost spherical,[9] which we consider in this article. Acoustic radiation forces then initiate bubble rise provided that:

$$\frac{1}{\sigma_Y}\underbrace{\left\langle \frac{F_z(\mathbf{x},t)}{2\pi R^2(t)} \right\rangle}_{\sigma_{ac}} = \frac{1}{3}\frac{R_0|\nabla p(\mathbf{x})|_\zeta}{\sigma_Y}|\cos(\phi)| \geq 5.1. \quad (11)$$

3 Materials and methods

3.1 Carbopol microgel preparation and properties

The yield-stress fluid we use in this article is a Carbopol ETD 2050 microgel (Lubrizol Corporation, Wickliffe, Ohio, USA) of concentration 0.15% w/v that has been extensively studied in the literature.[5,35–37] The Carbopol primary particles are made of crosslinked polyacrylic acid, which swells at high pH to form a jammed assembly of soft particles with a diameter of several microns.[36]

Following classical preparation protocols,[5,37] we first let the Carbopol flakes dissolve in MilliQ water (18.2 MΩ cm) for 1 hour under gentle agitation before adding 1% v/v 1 M NaOH to adjust the pH to 7. The fluid is then stirred for 20 minutes by an overhead mixer (RW 20 fitted with a R1303 dissolver impeller, IKA, Staufen im Breisgau, Germany) at 2000 rpm. We then place the fluid in a vacuum chamber until all bubbles that have been incorporated during mixing are removed. The fluid is finally left to equilibrate overnight.

We characterise the rheology of the Carbopol microgel using a rotational rheometer (MCR 302, Anton Paar, Graz, Austria). We perform flow curves and oscillatory measurements, from which we deduce σ_Y and G following standard fits;[1] both data series are displayed in Appendix A. We measure the sound velocity in the fluid c using a separate acoustic setup. We assume that its density is equal to that of water at room temperature and we choose a surface tension Γ based on dedicated experiments eliminating the impact of elastic stresses.[38] We finally use the standard heat diffusivity D of air from classical sources[39] to compute the thermal dissipation coefficient κ' from Section 2.1. The values of these parameters are compiled in Table 1.

3.2 Ultrasound excitation and high-speed imaging

Our experiments take place in a parallelepipedic container filled with the yield-stress fluid, as sketched in Fig. 1. The walls of the containers are either made of glass or duralumin, ensuring total internal reflection of the incident acoustic wave. A lid fitted with needles partially dipped in the fluid is used at the top of the device to prevent sloshing while maintaining the total internal reflection with air.

We apply acoustic excitations using a Langevin transducer (Steminc, Doral, Florida, U.S.A.) oscillating between f = 19.45 and 29.2 kHz. We drive the transducer using a waveform

Table 1 Physical parameters of bubble oscillation in Carbopol. Source of the data: n, K, σ_Y, G and c have been measured by the authors. The surface tension Γ and the heat diffusivity D and taken from ref. 38 and 39 respectively. The polytropic index κ is computed following ref. 24

Name	Fluid	Symbol	Value	Unit
Polytropic index		κ	1.30	
Ambient pressure	Air	p_0	1.013×10^5	Pa
Heat diffusivity	Air	D	1.9×10^{-5}	$m^2\ s^{-1}$
Viscosity	Water	η_0	1.0×10^{-3}	Pa s
Specific gravity	Water	ρ	9.98×10^2	$kg\ m^{-3}$
Sound velocity	Carbopol	c	1.495×10^3	$m\ s^{-1}$
Surface tension	Carbopol	Γ	6.2×10^{-2}	$N\ m^{-1}$
Flow index	Carbopol	n	0.36	
Flow consistency	Carbopol	K	5.0	$Pa\ s^n$
Yield stress	Carbopol	σ_Y	5.3	Pa
Shear modulus	Carbopol	G	36.0	Pa

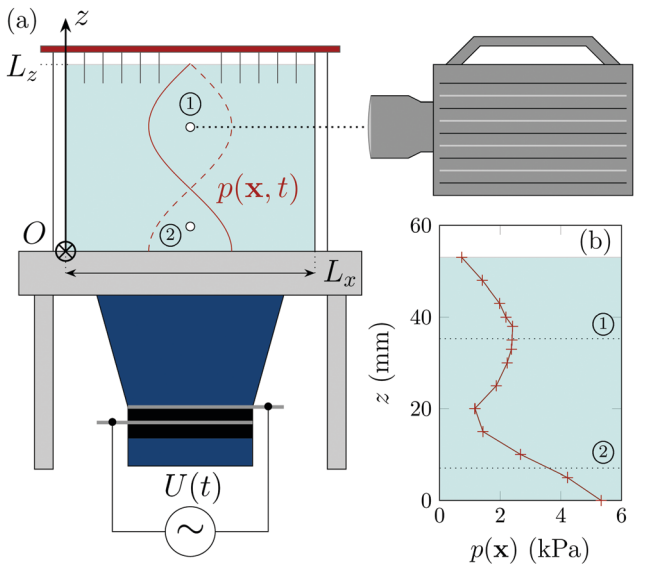

Fig. 1 (a) Schematic diagram of the experiment. A Langevin transducer (in blue) provides an acoustic excitation to the yield-stress fluid container above it. The excitation frequency f matches the resonance of the transducer and that of a (0, 0, 3/2) standing wave pattern $p(\mathbf{x},t)$ inside the container. Bubbles of interest are illuminated by an optical fibre facing the high-speed camera (right, in grey). (b) Vertical pressure profile in water at the centre of the setup for a frequency f = 21.5 kHz, an applied voltage U = 5.0 V and a fluid height L_z = 5.3 cm. We report the vertical positions of locations ① and ② (dashed lines).

generator (33210A, Agilent, Santa Clara, USA) coupled to a linear amplifier (AG 1021, T&C Power Conversion, Rochester, USA). The amplifier gain controls the voltage U applied to the transducer and ultimately the applied pressure amplitude $p(\mathbf{x},t)$ during the experiment. We always work at relatively low input voltage and amplifier gain to prevent non-linear distortion of the amplifier or transducer response.

The container dimensions L_x = 10.2 cm, L_y = 5 cm, and L_z are adapted to produce a resonant standing wave pattern at the applied frequency f, where the pressure amplitude $p(\mathbf{x})$ varies mostly alongside $\mathbf{e_z}$. This pattern, shown in Fig. 1(a), corresponds to the (0, 0, 3/2) room mode of the container.[40] Pressure measurements using a polyvinylidene fluoride hydrophone

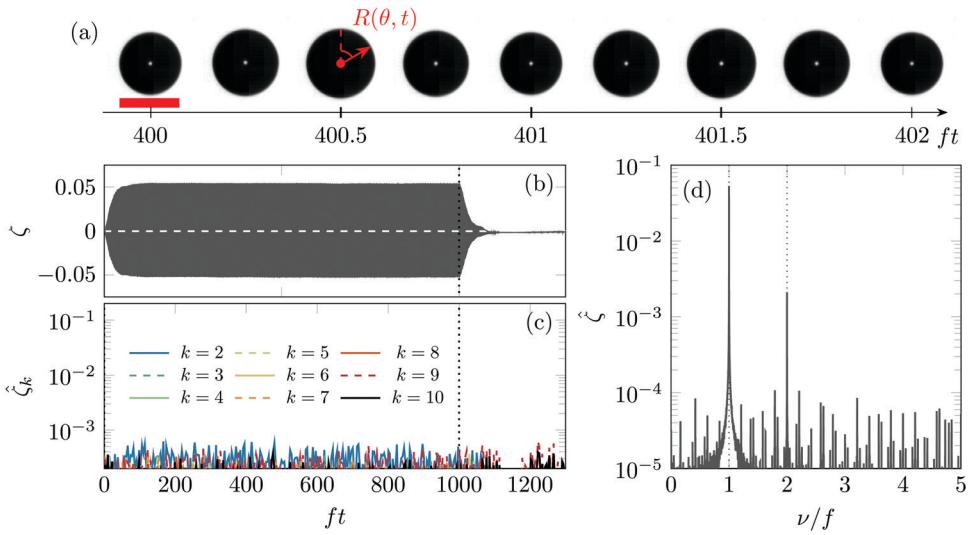

Fig. 2 Linear oscillation of a bubble in a yield-stress fluid under acoustic excitation at a frequency f = 21.5 kHz. (a) Snapshots of the bubble oscillation during two oscillation cycles. The red scale bar is 250 μm. (b) Time series of the relative departure from the initial radius $\zeta(t)$ as a function of time. Acoustic excitation starts at ft = 0 and stops at ft = 1000, marked by a dotted line. (c) Spectrogram $\hat{\zeta}_k(t)$ of the bubble shape modes for $k \leq 10$, showing no notable shape oscillation content at $f/2$. (d) Complex modulus of the Fourier transform of $\hat{\zeta}$.

(RP 42s, RP Acoustics, Leutenbach, Germany) along the vertical line at the centre of the container [presented in Fig. 1(b)] are compatible with the predicted room mode; they also show that the distortion level is small. We then define two locations named ① and ② (see Fig. 1). The first location corresponds to the pressure anti-node at two-thirds of the cell height for which the pressure gradient $\nabla p(\mathbf{x}_1)$ is zero. It is used in Sections 4.1 and 4.2. The second location is chosen below the pressure node to achieve both a significant pressure and pressure gradient so as to maximise acoustic radiation forces, as explained in Section 2.2. At this location and for an applied frequency f = 19.45 kHz used throughout Section 4.3, we measure a relative pressure gradient $|\nabla p(\mathbf{x}_2)/p(\mathbf{x}_2)|$ in the vertical direction equal to 82 m^{-1}. Given the efficiency of the resonant setup $p(\mathbf{x}_2)/U$ = 0.13 kPa V^{-1} at this location, the acoustic pressure gradient $|\nabla p(\mathbf{x}_2)|$ exceeds the hydrostatic pressure gradient for voltages $U \geq 1$ V.

We align the high-speed camera (Fastcam SA5, Photron, Tokyo, Japan) at location 1 or 2 by imaging the tip of the hydrophone. We then remove the hydrophone and inject a bubble of initial radius $\lesssim$300 μm with a small syringe in the frame of the camera before fine-tuning its position through careful manual pushing. Such a procedure inevitably modifies the internal stresses of the fluid around the bubble. Following ref. 26, we consider the slow bubble dissolution (reported in ESI,† Section S2) as a sweep over the initial bubble radii R_0 and we then produce a resonance curve [eqn (3b)] for a constant frequency f and varying R_0. At the start of the camera acquisition, a burst of N = 200 to 3000 sinusoidal cycles is sent by the waveform generator to the amplifier and the transducer. The camera records images up to 250 000 frames per second, corresponding to ∼10 images per oscillation period. We set the total acquisition time to measure both the bubble response to the acoustic excitation and its subsequent relaxation. We report in our acquisitions a small source of vibration at f = 130 Hz. It impacts bubble position measurements but does not affect the measured bubble radius and shape.

3.3 Bubble contour detection and decomposition into Legendre and Fourier modes

The data processing of video acquisitions is inspired by two recent works.[16,41] In short, our Matlab routines normalise raw images and apply a luminosity threshold in order to retrieve the location of the bubble centroid $\mathbf{x}(t)$ and its mean radius $R(t) = R_0[1 + \zeta(t)]$ as a function of time.

We then perform a Fourier transform of the radius time series and pay a particular attention to $\hat{\zeta}(\nu)$ when ν is a multiple or a sub-multiple of the oscillation frequency f. Significant harmonic content indicates that we are no longer working in the linear bubble oscillation framework described in Section 2.

We also study whether bubbles remain spherical during the oscillations by examining the two-dimensional outline of the bubbles. To do so, we plot 360 lines originating at the bubble centroid, with equally spaced polar angles θ, defined from the vertical direction as shown in Fig. 2(a). We define the local bubble radius $R_0[1 + \zeta(\theta,t)]$ as the point where each line crosses the bubble edge. We then define the bubble orientation $\theta_0(t)$ as the angle for which $R(\theta_0 + \theta,t)$ lies closest to $R(\theta_0 - \theta,t)$. In earlier studies,[26,41–43] bubble outlines usually show a clear k-fold symmetry, which is empirically assumed to correspond to the degree, or mode, k of the spherical harmonics Y_k^m describing the three dimensional shape of the bubble. Following the same approach, we project the bubble shape outline $\zeta(\theta,t)$ on the Legendre polynomials of degree k, $P_k(\cos(\theta))$.[41] We may then define the instantaneous amplitude of a shape mode k, $\zeta_k(t)$:

$$\zeta_k(t) = \frac{2k+1}{2}\int_{-1}^{1} \zeta(\theta,t) P_k(u)\mathrm{d}u, \qquad (12)$$

using $u = \cos(\theta - \theta_0)$. This projection actually defines two integration paths, one for each bubble hemisphere. We choose to fit each hemisphere separately and define $\zeta_k(t)$ as the average of the two. We finally compute the spectrograms $\hat{\zeta}_k(\nu,t)$ of the bubble shape modes:

$$\hat{\zeta}_k(\nu,t) = \frac{2}{\Delta t}\left|\int_{t-\Delta t}^{t+\Delta t} \zeta_k(\tau)\exp(2i\pi\nu\tau)\mathrm{d}\tau\right| \quad (13)$$

We pay close attention to $\hat{\zeta}_k(t) = \hat{\zeta}_k(f/2,t)$, as $f/2$ is the frequency at which shape oscillations arise in Newtonian fluids and Kelvin–Voigt materials.[29,44] The time window size used to compute the spectrograms $\Delta t = 2/f$ allows us to capture this component accurately.

3.4 Characteristic quantities and dimensionless groups

The small bubbles ($75\ \mu\mathrm{m} \leq R_0 \leq 300\ \mu\mathrm{m}$) we consider in this article correspond to very small Bond–Eötvös numbers,

$$\mathrm{Bo} = \frac{\rho_l g {R_0}^2}{\Gamma} \leq 0.01, \quad (14)$$

and modest elasto-capillary numbers,

$$\mathrm{El} = \frac{G R_0}{\Gamma} \leq 0.17. \quad (15)$$

We then expect bubbles to remain spherical at rest, as hypothesised in Section 2. The yielding parameter for such bubbles is also small,

$$Y^{-1} = \frac{2\rho_l g R_0}{3\sigma_Y} = 0.26, \quad (16)$$

since the critical value ${Y_c}^{-1}$ needed to initiate the rise of spherical bubbles is 5.1.[9] We also provide a numerical estimate of the critical oscillation amplitude ζ_c required to initiate Carbopol yielding following eqn (10):

$$\zeta_c = \frac{1}{2\sqrt{3}}\frac{\sigma_Y}{G} = 0.043 \quad (17)$$

We can finally compute the ratio of the elasto-plastic cross-over time scale in the yielded material to that of the bubble oscillations, as defined in Section 2.3. We refer to it as the Deborah number of our experiments:

$$\mathrm{De} = 2\pi f\left(\frac{K}{G}\right)^{1/n} = 590 \gg 1. \quad (18)$$

Hence, even if the material has yielded, it will remain predominantly elastic, and we do not expect the bubble oscillations dynamics to be affected by yielding. However, if the material has yielded due to bubble oscillations, irreversible bubble displacement may occur due to buoyancy and acoustic radiation forces, which are applied continuously during $N \geq 1000$ cycles, resulting in a time scale ratio $f/N(K/G)^{1/n} = \mathrm{De}/2\pi N$ below unity.

We may lastly define the Péclet number comparing heat diffusion in the air to its advection due to bubble oscillations: $\mathrm{Pe} = 2\pi f {R_0}^2/D = 160$. For this range of Péclet numbers, thermal dissipation is the dominant contribution to the damping term β (see Appendix B) and the polytropic exponent is $\kappa = 1.30$.[24]

4 Experimental results

4.1 Linear response: general observations

We first show, for a typical experiment, the criteria we use to define spherical and linear bubble oscillations. Fig. 2(a) shows an image sequence of bubble oscillation after the end of the transient regime at location ①. We also show in Fig. 2(b) the bubble oscillation amplitude $\zeta(t)$, which highlights the typical time scale $\sim 100/f$ needed for the transient state to vanish. The bubble radius at rest before and long after the oscillations are equal, ruling out any significant gas diffusion into or out of the bubble. Fig. 2(c) confirms that bubbles remain spherical as the shape oscillation modes $\hat{\zeta}_k$ remain at a very low level before, during and after the acoustic excitation. We then set the noise threshold for shape oscillations to 10^{-3} for the rest of this article. Fig. 2(d) confirms the linearity in time of the bubble response. The bubble oscillation spectrum $\hat{\zeta}(\nu)$ shows a peak at $\nu = f$ and harmonic content is almost absent aside from a small peak at $\nu = 2f$. In all our experiments, spherical bubble oscillations are also linear in the time domain.

4.2 Resonance curve

We then measure the resonance curve [eqn (3b)] of bubbles in the linear regime, sweeping over their initial radius R_0. Fig. 3 highlights the excellent agreement between the measured oscillation amplitude ζ from a series of experiments conducted at a constant pressure amplitude and the prediction of eqn (3b). We first verify that the fitted pressure amplitude $p = 1.73$ kPa matches independent pressure measurements

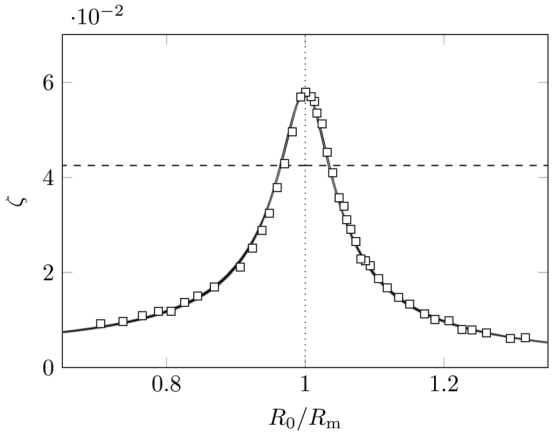

Fig. 3 Resonance curve of a bubble in Carbopol obtained for an oscillation frequency of 21.5 kHz and an acoustic pressure amplitude $p = 1.73$ kPa. The number of cycles has been set to 1000. The Minnaert resonance radius is $R_m = 148\ \mu\mathrm{m}$. The dashed horizontal line represents the onset of Carbopol yielding deduced from eqn (10). Squares represent experimental data. The solid black line is a fit of the linear data following eqn (3b), with two free parameters, the solvent viscosity η_s (included in the damping term β) and the applied pressure p. The 95% confidence interval region is smaller than the size of the markers.

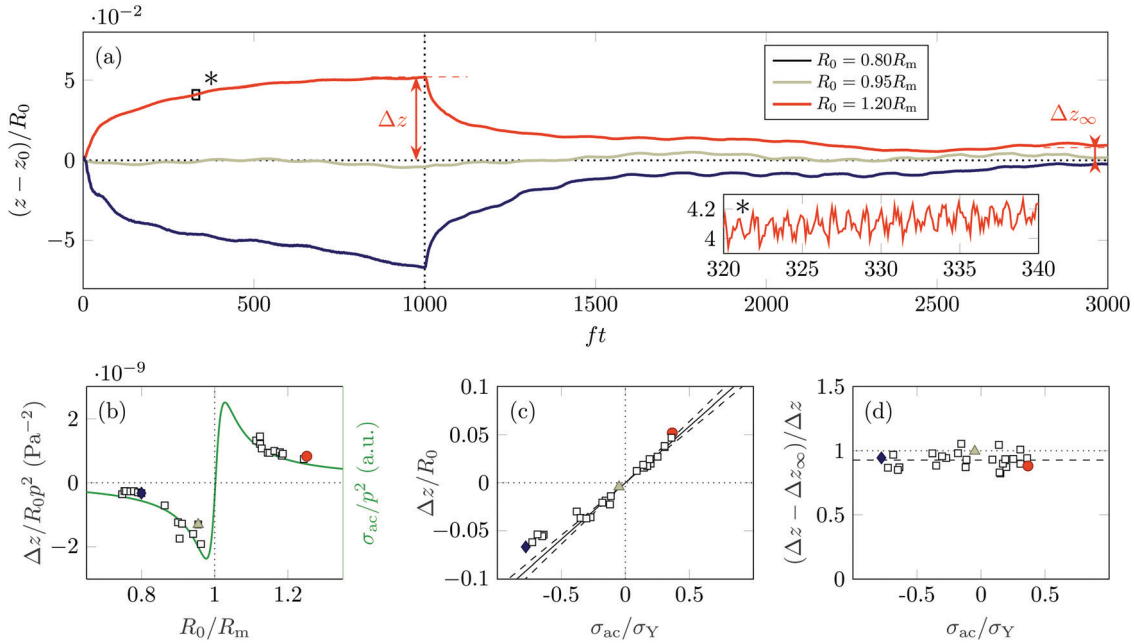

Fig. 4 Displacement of the bubble centroid in the vertical direction for spherical bubble oscillation experiments conducted at f = 19.45 kHz. The Minnaert resonance radius is R_m = 163 μm. (a) Normalised bubble vertical displacement as a function of time for three experiments: $R_0 \simeq 1.2R_m$ (red), $R_0 \simeq 0.95R_m$ (light grey) and $R_0 \simeq 0.8R_m$ (blue). Data have been averaged over an oscillation period. Inset: Raw temporal profile of the bubble vertical position highlighting the oscillating part of the signal. (b) Typical strain applied by the bubble net motion for an applied pressure of 1 Pa, $\Delta z/R_0p^2$ (markers), superposed with the expected acoustic radiation stress applied to the bubbles σ_{ac}/p^2 (solid line, see main text) also for p = 1 Pa. Note the separate y axes. (c) Local rheology of the fluid: typical measured strain $\Delta z/R_0$ plotted as a function of the acoustic radiation stress normalised by the yield stress σ_{ac}/σ_Y. The solid line is the best linear fit of the data for $|\sigma_{ac}/\sigma_Y| < 0.5$ and the dashed lines show the linear fits from the boundaries of the 95% confidence interval. (d) Recovery after strain of the bubble: the amount of recovered strain $(\Delta z - \Delta z_\infty)/\Delta z$ long after the end of acoustic excitation is plotted as a function of the normalised acoustic radiation stress. In Panels (b)–(d), the red, light grey and red markers correspond to the three lines of Panel (a).

using the hydrophone (data not shown). All experiments show neither any significant shape oscillation nor any non-linear behaviour in the time domain. By fitting the solvent viscosity to the data, and estimating uncertainties on thermal and acoustic damping from eqn (6), as detailed in ESI,† Section S1, we obtain an estimate for the solvent viscosity, η_s = 1.3 ± 3.0 mPa s, compatible with the viscosity of water η_0 = 1.0 mPa s, in agreement with the assumptions of the rheological model.[21] Other sets of data (not shown) performed at 19.45 ≤ f ≤ 29.2 kHz are less precise but systematically include the viscosity of water in their confidence intervals.

Close to $R_0 = R_m$, the experiments in Fig. 3 satisfy the yielding criterion $\zeta \geq \zeta_c$, yet follow the exact same trend as the other experiments. Material yielding has therefore no impact on the bubble dynamics. This result confirms the prediction made in Sections 2.3 and 3.4 that elastic stresses do not have time to relax in the yielded material and on the time scale of the oscillations. More surprisingly, we note that none of the experiments for which yielding is expected shows any noticeable displacement of the centre of the bubble.

4.3 Response to acoustic radiation forces

In Section 4.2 we did not observe any significant displacement of bubbles driven into oscillations at location ①, where they are subject only to the buoyancy force. Next we test the effect of acoustic radiation forces [eqn (11)] on bubble displacement, by looking at bubbles positioned at location ② where they are subject also to acoustic pressure gradients.

Fig. 4(a) shows the vertical position of the bubble centroid $z(t)$ for three experiments. Bubbles smaller (respectively larger) than the resonant radius R_m show a net downwards (respectively upwards) motion towards the pressure anti-node (respectively pressure node), in line with the change of sign of cos(ϕ) in eqn (3c). The inset of Fig. 4(a) highlights the zero-average oscillatory part of the acoustic radiation forces [averaged out in eqn (7)], clearly noticeable and superposed with the slower displacement related to the Bjerknes force.

Bubble trajectories are non-trivial: they cannot be fitted by a simple exponential law related to the Kelvin–Voigt solid viscoelastic relaxation time $ft_{KV} = \eta_s/G$, which amounts to less than one oscillation cycle, nor to the time needed for the transient regime to die out, which corresponds to around 100 cycles, or even the typical elasto-plastic relaxation time of the yielded material, given by De/2πN = 1, also close to N = 100 cycles (see Fig. 2). We can rule out viscous or plastic responses of the fluid as the bubble centroid does not reach a constant, finite velocity dz/dt. They are however not long enough to be completely conclusive regarding more complex, non-linear responses of the fluid, such as creep.[5]

Fig. 4(b) examines the sensitivity of bubbles to acoustic radiation forces as a function of their size, defined as the normalised displacement $\Delta z/R_0p^2$ as Bjerknes forces are

quadratic in pressure amplitude (see Section 2.2). Our experimental data superposes well with the theoretical expression for the average stress applied onto the bubble σ_{ac}/p^2 from eqn (3b), (3c) and (7), which suggests a linear relation between bubble stress and strain.

Fig. 4(c) directly plots the acoustic radiation strain $\Delta z/R_0$ as a function of the corresponding stress, normalised here by the yield stress σ_Y. We compute here the stress using experimental values of ζ, R_0, p and $|\nabla p|$ and we choose $\cos(\phi)$ based on eqn (3c). The data confirms the linear trend suggested from Fig. 4(b) at low applied stresses and shows a noticeable non-linear deviation for higher stresses. As yielding due to the oscillation amplitude has no impact on the bubble mobility (see ESI,† Section S3), this deviation may only stem from a non-linear behaviour of the emission setup or non-linear elasticity of the Carbopol. We measure the slope of the linear trend at low stress in Fig. 4(c) to extract an estimate of the linear elastic modulus of the surrounding medium $G = 44.4 \pm 3.5$ Pa, following eqn (8). This value is in fair agreement with that obtained from bulk oscillatory rheology, $G = 36.0$ Pa.

Fig. 4(d) shows the recovered strain 2000 cycles after the end of the acoustic excitation. The recovery is close to 100% for all experiments, which confirms the elastic nature of the deformation shown in Fig. 4(c) expected for experiments conducted for $\sigma_{ac}/\sigma_Y \leq 5.1$. Irreversible bubble motion can then only be achieved for higher applied pressure and oscillation amplitude ζ. As we will see in Section 4.4, we could not perform such experiments due to the onset of bubble shape oscillations.

4.4 Shape oscillations

4.4.1 Critical pressure and observed modes. In Newtonian fluids and soft solids, shape oscillations of mode number k may grow when the applied pressure p exceeds a critical value $p_{c,k}$, which depends on R_0, the applied frequency f and the material properties.[44,45] For a fixed driving frequency f, these predictions define regions in the (R_0,p) plane in which bubble oscillations either remain spherical, allow the growth of a single shape mode k, or allow multiple shape modes. Linear instability predictions for shape oscillations in Kelvin–Voigt soft solids have recently been derived;[44] they are recalled in Appendix C. In Newtonian fluids, experimental results match the linear instability predictions fairly well.[42,46,47] In contrast, numerical[48] and experimental[26] data on the onset of bubble shape oscillations in non-Newtonian fluids are scarce and not yet conclusive.

Fig. 5 highlights four shape oscillation modes $4 \leq k \leq 7$ that have been clearly identified in experiments at location ①. Less than half of the experimental data is sufficiently clear to define unambiguously a shape mode number k. Several experiments (see last row of Fig. 5) instead show a complex outline, which likely results from the projection in the imaging plane of a three-dimensional mode Y_k^m with $m \neq \{0, k, -k\}$ and a random orientation. In all cases, the frequency of the shape oscillations is $f/2$, confirming that shape oscillations also result from a sub-harmonic instability in yield-stress fluids.

We report in Fig. 6 the shape oscillations observed as a function of both R_0 and p for seven slowly dissolving bubbles,

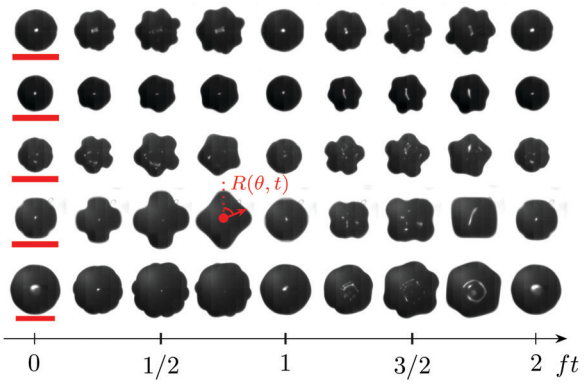

Fig. 5 Shape oscillation modes observed in our experiments, shown for two oscillation periods ($2/f$). From top to bottom, the applied frequency is $f = 27.94$ kHz, $f = 29.2$ kHz, $f = 27.94$ kHz, $f = 19.45$ kHz and $f = 19.45$ kHz. The first four rows show shape oscillations with clear modes $k = 7$, 6, 5 and 4 respectively. The last row shows an experiment for which shape oscillations are clearly detected but the corresponding mode k is difficult to ascertain. The red scale bars are 300 μm.

identified by a roman numeral from i to vii. Multiple acquisitions have been conducted on each bubble, with the pressure p kept constant throughout their dissolution. The critical pressure of shape oscillations reaches a single local minimum close to $R_0 = R_m$; further away from R_m, it quickly grows and ultimately exceeds the maximum pressure achieved in our setup for $R_0 \leq 0.8R_m$ and $R_0 \geq 1.3R_m$. Our data indicates that the shape number k in our experiments increases with R_0, in qualitative agreement with models[44,45] and experiments in Newtonian fluids.[42,47]

We overlay in Fig. 6 the predicted critical pressure $p_{c,k}$ derived in Appendix C by combining eqn (3b) and the critical bubble oscillation amplitude $\zeta_{c,k}$ above which spherical oscillations are linearly unstable. We choose the value of the viscosity we fitted in Section 4.2, $\eta_s = 1.3$ mPa s and the elastic modulus measured in Section 4.3, $G = 44.4$ Pa. A large amount of experiments shows stable spherical oscillations whereas the model predicts they are linearly unstable with respect to shape oscillation modes 4 to 8. The model however correctly predicts that modes 5 and 6 are favoured for $R \simeq R_m$ in agreement with the low values of $p_{c,5}$ and $p_{c,6}$ in this region.

4.4.2 Impact on net bubble motion. In Newtonian fluids, bubble shape oscillations are closely related to an unpredictable, dancing[49] motion of their centre of gravity. This motion stems from a non-linear interaction with both spherical oscillations and other shape modes.[49] In the context of bubble removal, we wish to understand the impact of shape oscillations and dancing motion on the ability of ultrasound devices to push and pull bubbles irreversibly in yield-stress fluids.

Fig. 7 shows the strong impact of shape oscillations on bubble motion. The first three bubbles [Fig. 7(a–f)] show motion towards an antinode in agreement with their initial size $R_0 \leq R_m$. The presence of a clear shape mode enhances bubble mobility, as shown in Fig. 7(c and d) for $k = 4$. We also observe spurious motion in the direction transverse to the pressure gradient when a single bubble shape mode k is no

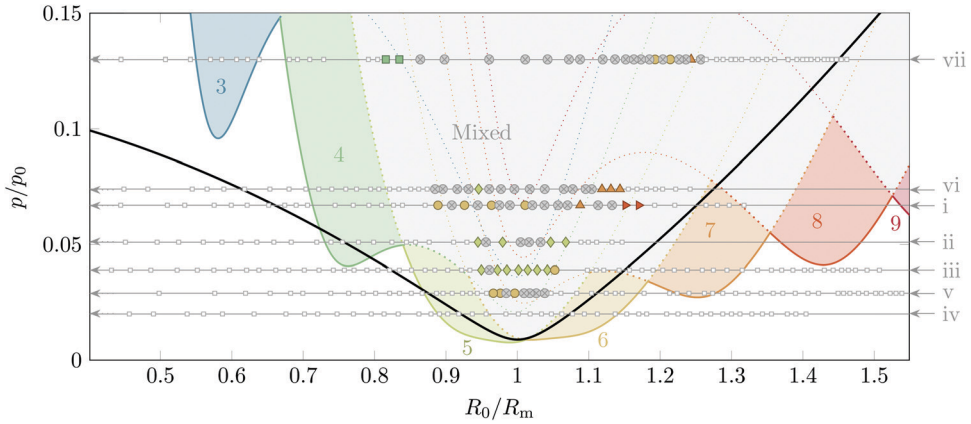

Fig. 6 Phase diagram for bubble shape oscillations as a function of the applied pressure p/p_0 and the initial radius of bubbles R_0/R_m for an excitation frequency f = 22.5 kHz. Experimental data have been acquired throughout the dissolution of seven bubbles, identified with roman numerals i to vii from earliest to latest data series. As the applied pressure p is kept constant for each bubble, the seven data series form horizontal series of points, starting from high values of R_0 and ending for low values of R_0, following the direction of the grey arrows. Individual acquisitions for each data series are shown as symbols. The modes that we could define without any ambiguity are plotted as red rightwards pointing triangles (k = 8), orange upwards pointing triangles (k = 7), yellow circles (k = 6), light green diamonds (k = 5) and green squares (k = 4). Most acquisitions with shape oscillations have a non-clear mode [*e.g.* last row of Fig. 5]; they are plotted as crossed circles. The small white squares represent stable spherical oscillations. The critical pressure for each shape mode, computed from ref. 44 and eqn (3b), is shown as a line with the same colour coding as the experiments. Above these lines lie coloured regions where only one oscillation mode k can grow, and a broader grey region where multiple shape modes may grow. The black solid line depicts the threshold for fluid yielding defined combining eqn (3b) and (10).

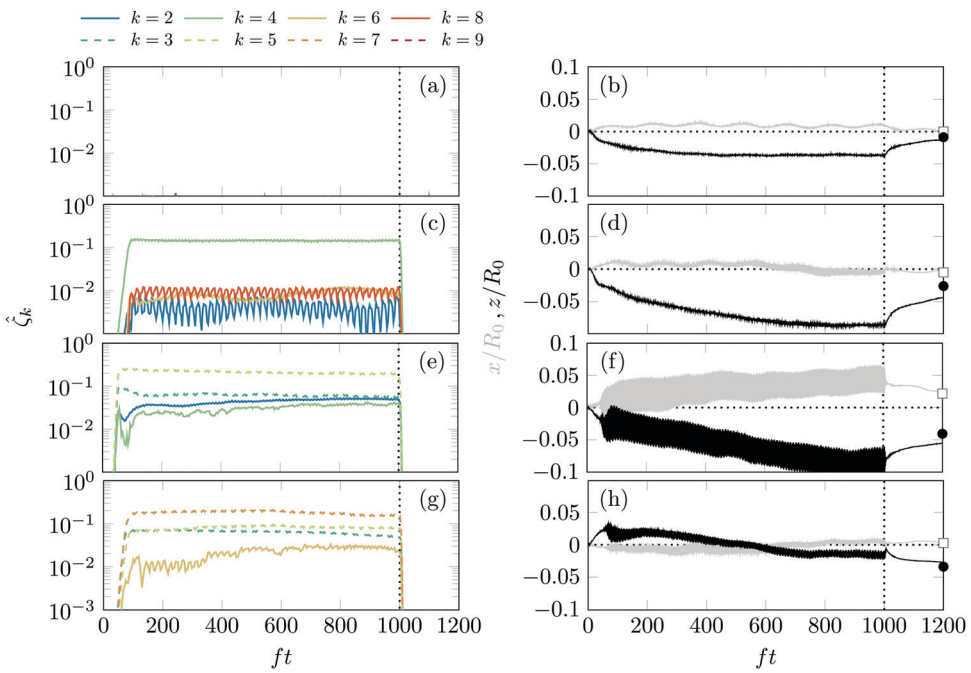

Fig. 7 Analysing experiments for which one or several shape oscillation modes are observed and steady. Panels (a, c, e and g), spectrograms of the recorded shape mode intensity as a function of time for an experiment with no shape oscillation (a), a clearly identified mode k = 4 (c) and two experiments (e and g) for which the shape modes are not clearly identified. The acoustic excitation starts at t = 0 and stops at ft = 1000, marked by a dotted line. Only the four most prominent projection modes are shown. Panels (b, d, f and h), net bubble motion corresponding to the spectrograms of Panels (a, c, e and g). The grey line shows the relative displacement along the x (horizontal) axis while the black line shows its z (vertical) counterpart. The white square and the black circle respectively represent the position of the bubble in the x and z axes at $ft \simeq 3100$, long after the oscillations have stopped.

longer clearly identified [as seen in Fig. 7(e and f)]. We also have observed reversals of the bubble direction of motion following the onset of shape oscillations [Fig. 7(g and h)]. In general we conclude that while shape oscillations increase bubble displacement, the direction of motion can no longer be controlled.

5 Discussion

5.1 Precision and relevance of the solvent viscosity measurement

The experimental bubble oscillation amplitude ζ in the linear regime may be fitted to the theoretical resonance curve to extract the oscillation damping parameter β. After carefully subtracting from β the dominant acoustic and thermal contributions, we measure a fluid viscosity η_s = 1.3 mPa s. An analysis of the fitting procedure and the uncertainties on β shows that this value is not statistically different from the viscosity of water used as the solvent here, and in agreement with the rheological model.[20,21] This low value seems surprising considering the bulk oscillatory rheology of Carbopol (see Appendix A) which rather suggests a viscosity $G''/2\pi f \simeq 1$ Pa s in the linear regime for low frequencies f = 1 Hz, while the Kelvin–Voigt model we use assumes a constant viscosity below yielding for all frequencies.

Indeed, real hydrogels and yield-stress fluids under oscillatory shear do not show a constant viscosity as a function of f: classical rheological measurements show that their loss modulus G'' behaves as a constant or as slowly increasing power laws of f[50] leading to a decreasing viscosity $G''/2\pi f$. These power law scalings may be reproduced by fractional derivative models[50] but their microscopic origin remain insufficiently understood.[7] The value of the viscosity deduced from G'' in oscillatory rheology may therefore not be particularly meaningful. In contrast, viscous or close-to-viscous scaling of the stress has been experimentally observed in yield-stress fluids at high frequencies and strain rates.[51,52] At such frequencies, dissipation due to the solvent, scaling as $\eta_s f$, may become the dominant contribution to G'', and the material could then recover a Kelvin–Voigt rheology. Our results suggest that bubble oscillations experiments fit into this high-frequency limit and allow a proper measurement of the solvent viscosity.

5.2 Linear response to Bjerknes forces

We have used in Section 4.3 the constant (or zero-frequency) part of the acoustic radiation force to perform an equivalent of step-stress tests, but at a local scale R_0. For moderate acoustic stresses $\sigma_{ac} \leq \sigma_Y$, we measure a linear strain–stress relation at the end of oscillations, from which we deduce an independent measurement of the local linear elastic modulus of the fluid below yielding, G = 44.4 ± 3.5 Pa, comparable to that obtained using bulk rheology, G = 36 Pa. All quantities used to derive G are either directly measured or estimated from the resonance curve: hence, in contrast with previous works,[53] our measurement is truly independent from bulk rheology.

The complex time dependence of the displacement shown in Fig. 4(a) is reminiscent of creep behaviour.[5] Creep is however usually associated to irreversible strain and a non-linear stress–strain relation in bulk rheology experiments, both of which are not observed here. Interestingly, fully reversible creep motion up to the yield point has also been reported in experiments in which acoustic radiation forces are used to push small spheres.[53] The relatively small pressure gradients applied in our experiments according to eqn (11) then cannot alone initiate bubble rise. Performing experiments of longer duration may reveal whether the response to acoustic radiation forces indeed follows a power law or an exponential profile with time, which could be helpful to validate the recent, advanced models of yield-stress fluids.[7,8]

5.3 Absence of irreversible rising motion

Several experiments satisfy the bubble oscillation yielding criterion $\zeta \geq \zeta_c$ and apply acoustic radiation stresses σ_{ac} comparable with the yield stress for a sufficiently long time to let elastic stresses relax. Yet, they do not suffice to induce irreversible bubble motion and we do not observe the finite average rising speed predicted in the recent numerical simulations of ref. 19. The yielding criterion ζ_c = 0.043 we have derived is then a necessary condition, but not sufficient, to induce bubble rise at a useful rate for removal applications.

One explanation for this lack of irreversible motion is that the steady-state bubble rise velocity is too small to be observed. Firstly, the yielded region remains under 1.25 times the size of the bubble radius, increasing drag by a factor 40 compared to the unconfined case.[54] Secondly, the plastic viscosity in the yielded material stays significantly higher than the solvent viscosity. The corresponding rising velocities may therefore be too small to be resolved in experiments.

Additional factors may prevent irreversible rising motion. For instance, the von Mises yield criterion [eqn (10)] has been shown to fail for bulk yielding in extension, as already reported in other simple yield-stress fluids.[55–57] Another possibility lies in finite-size effects given the relatively small size of the bubble compared to the constitutive elements of Carbopol. Local restructuration around slowly-growing bubbles has been recently evidenced in sparse networks of microfibrillated cellulose, which impacts their bubble retention capacity.[58] It is difficult to know at the moment whether this scenario applies in our case, since Carbopol is soft-jammed and isotropic and the strain rates at play are high. We may finally question the relevance of the very notions of yielding and unyielding in our experiment since the oscillation timescale $1/f$ can be below that of the microscopic plastic rearrangements used in yield-stress fluids models.[7,8]

5.4 Nature and onset of shape oscillations

The critical pressure $p_c{}^k$ above which we experimentally observe shape oscillations is significantly higher in Carbopol thant what we expect from a linear instability analysis in Kelvin–Voigt materials[44] if we use the fluid properties we derived in Sections 4.2 and 4.3. Yield-stress fluids are known to exhibit residual stresses at rest, with unknown spatial distribution. We expect non-homogeneous residual stresses around the bubble to impact bubble shape oscillations by altering the critical pressure $p_{c,k}$ depending on the compatibility between the geometry of the shape modes and that of the residual stresses. Further analysis of the bubble shapes, conducted in ESI,† Section S4, shows that residual stresses induce a very small (0.5%) residual deformation of the bubble

at rest. Under acoustic excitation, the bubble shape modes do neither respect the orientation nor the symmetry of these residual deformations. Hence we do not observe any direct impact of residual stresses on bubble shape oscillations even though we cannot rule out their influence. Using a solvent with a higher viscosity in experiments would be particularly helpful to either reconcile experimental data with the linear instability model[44] or to prove that it is not applicable to yield-stress fluids.

5.5 Consequences on acoustic bubble removal performance

Shape oscillations imply unpredictable bubble motion that inevitably reduces the efficiency of any directed motion induced by acoustic radiation forces or bubble buoyancy. We notice that the window of operation for bubble removal, lying above the black line and below the coloured symbols of Fig. 6, is limited especially since the yielding criterion of eqn (10) does not warrant bubble rise. Bubble removal using acoustic excitation in Carbopol could then be performed using stronger pressure gradients, for instance using focused ultrasound beams. We suspect Carbopol is particularly resistant to the removal process due to its very wide linear elastic regime, as shown in bulk rheology (Appendix A). Bubble removal should be easier in almost any other yield-stress fluid as they break down under much smaller strains.[59,60] Increasing η_s could also improve bubble removal by raising the critical pressure at which shape oscillations arise.

6 Conclusion

In this article, we have investigated how a small bubble oscillating at a high frequency interacts with Carbopol, a model yield-stress fluid. Bubbles of different sizes allow us to perform bubble spectroscopy[25,26] and extract a viscosity $\eta_s = 1.3$ mPa s of the fluid at high frequency and for a finite extensional deformation, in agreement with the solvent viscosity of water and as expected from a previous numerical study.[20] We have also used pressure gradients to apply acoustic radiation forces on bubbles, from which we measure the local linear shear modulus of the fluid $G = 44.4$ Pa, in fair agreement with bulk rheology. As long as the oscillations remain spherical, bubble motion is fully reversible given the range of acoustic radiation stresses $|\sigma_{ac}| \leq \sigma_Y$ achieved in our experiment. In particular, motion reversibility appears unaffected by the oscillatory yielding criterion derived by De Corato *et al.*[20]

Experiments performed at higher pressure always resulted in non-spherical shape oscillations. As shape oscillations result in an unpredictable bubble motion in all directions, acoustic bubble removal is quite inefficient in Carbopol. Future studies should explore the applicability of acoustic bubble removal in more fragile networks, corresponding to a wide range of attractive colloidal and athermal yield stress fluids in which spherical bubble oscillations largely beyond the yield point are possible, resulting in a strong decrease of both bubble confinement and plastic viscosity during its assisted motion.

Conflicts of interest

There are no conflicts to declare.

Appendix

A Carbopol rheology

We characterise the rheology the Carbopol microgel using a standard rotational rheometer (MCR 302) working with a cone-plate geometry fitted with sandpaper discs (grit P1500) to suppress wall slip. Before every test, we apply a pre-shear step at $\dot{\gamma} = 1500\ s^{-1}$ for 30 s and a rest step at $\sigma = 0$ Pa for 20 s. We perform two consecutive flow curves for decreasing and increasing shear rates $\dot{\gamma}$ between $0.001\ s^{-1}$ and $1500\ s^{-1}$, choosing 5 s steps and 10 points per decade. Amplitude sweeps are conducted at a frequency of 1 Hz for increasing shear strains γ between 0.01% to 1000%, and we choose to acquire 15 points per decade and average over 10 oscillation cycles. Our data are presented in Fig. 8.

Fig. 8(a) shows the flow curves of the fluid. The data fit to a Herschel–Bulkley law, $\sigma = \sigma_Y + K\dot{\gamma}^n$ is fair and yields $n = 0.36$, $K = 5.0$ Pa s^n, and $\sigma_Y = 5.3$ Pa. The two consecutive flow curves superpose well, meaning that fluid thixotropy is negligible. In Fig. 8(b), we identify the linear modulus of the Carbopol G

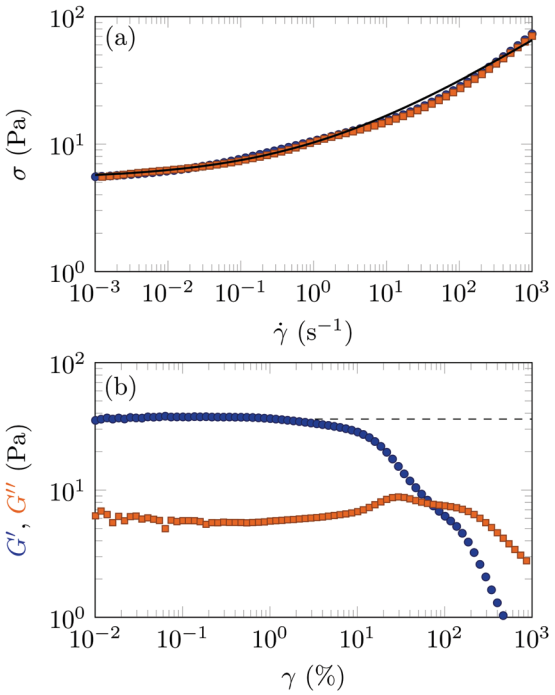

Fig. 8 Rheology of the Carbopol microgel. (a) Flow curve. Circles, decreasing shear rates, and squares, increasing shear rates, performed right after the blue circles. The black line represents the best fit to a Herschel–Bulkley law. (b) Oscillatory rheology: amplitude sweep starting from low strain amplitude at $f = 1$ Hz. Circles represent the storage modulus G' while squares show the loss modulus G''. The black dashed line represents the average value of the storage modulus in the elastic plateau, $G' = 36$ Pa.

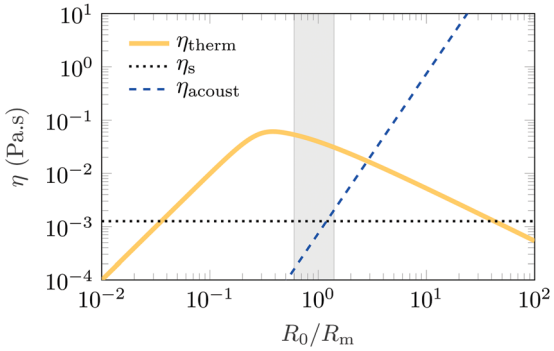

Fig. 9 Thermal, viscous and acoustic damping under linear bubble oscillation plotted as effective viscosities for an applied frequency f = 22.5 kHz. The thermal and acoustic contributions are directly plotted from eqn (6), while the value of η_s has been fitted to the resonance curve in Section 4.2. The greyed out region is our usual operating range.

with the storage part of the elastic modulus G' in the linear visco-elastic plateau for which $G' \gg G''$; this plateau spans from $\gamma \geq 0.01\%$ to $\gamma = 10\%$. We obtain $G = 36.0$ Pa. We also notice that the storage modulus is rather insensitive to the applied frequency f in the range accessible to the rheometer, 0.1 Hz to 10 Hz (data not shown).

B Contributions to damping of bubble oscillations

We compare in Fig. 9 the relative magnitude of the three contributions to dissipation detailed in eqn (6). We respectively note:

$$\eta_{\mathrm{therm}} = \frac{3p_0\kappa'}{8\pi f} \qquad \eta_{\mathrm{acoust}} = \frac{\pi^2\rho f^2 R_0^3}{4c} \tag{19}$$

and we plot η_{therm}, η_{acoust} and η_s for a solvent viscosity η_s = 1.3 mPa s deduced from Section 4.2. While acoustic damping is smaller than the viscous term in our operating range, thermal damping dominates them both and is up to 50 times higher than the viscous contribution. As we fit η_s by subtracting thermal dissipation η_{therm} and acoustic dissipation η_{acoust} from the total damping term β in the resonance curves, the solvent viscosity η_s fluctuates greatly for relatively small relative changes in η_{therm} and, to a lesser extent, in η_{acoust}. Obtaining a reliable value of the viscosity η_s then necessitates very high-quality resonance curve data and precise values of all the physical quantities present in thermal and acoustic damping, which are: p_0, R_0, ρ, c and D through the Péclet number in κ'. Uncertainties on both η_{therm} and η_{acoust} have been estimated in ESI,† Section S1. The lack of precise measurements on the thermal diffusion coefficient D results in a significant uncertainty on η_{therm}, of the same order as η_s, while the uncertainty on η_{acoust} remains negligible.

C Threshold for shape oscillations in soft materials

We recall here the predictions of ref. 44, who derived the critical bubble oscillation amplitude above which shape oscillations may be observed in a neo-Hookean, Kelvin–Voigt viscoelastic solid. Defining intermediate quantities:

$$\lambda_1 = 4(k-1)(k+1)(k+2)\frac{\Gamma}{4\pi^2 f^2 \rho R_0^3} \tag{20}$$

$$\lambda_2 = 2(k+2)(2k+1)\frac{\eta_s}{2\pi f \rho R_0^2} \tag{21}$$

$$\lambda_3 = 4(k+1)\frac{G}{4\pi^2 f^2 \rho R_0^2} \tag{22}$$

$$\lambda_4 = 12k(k+2)\frac{\eta_s}{2\pi f \rho R_0^2} \tag{23}$$

The critical amplitude $\zeta_{c,k}$ above which a shape mode k develops may be expressed as:

$$\zeta_{c,k}{}^2 = \frac{\left[(\lambda_1 - 1) + \lambda_3\left(4 + 4k/3 + k^2/3\right)\right]^2 + 4\lambda_2{}^2}{\left[(2k+1) - 3/2\lambda_1 + 2\lambda_2{}^2 - \lambda_3(18 + 19k/3 + k^2/3)\right]^2 + \lambda_4{}^2} \tag{24}$$

Since our experiments show that bubble oscillations up to the shape oscillation threshold are linear in the time domain, we may combine eqn (3b) and (24) to derive explicitly the critical pressure $p_{c,k}$ for all modes k. One surprising consequence of eqn (24) is that, despite modelling the three-dimensional growth of spherical harmonics Y_k^m generally defined by two shape modes k and m, the critical pressure of the model is independent of m.

Close to $R_0 = R_{\mathrm{m}}$, the critical pressure $p_{c,k}$ reaches a minimum for all modes k because it corresponds to the resonance condition of spherical oscillations. In addition, shape modes have a natural oscillation frequency, given by:

$$\pi^2 f^2 = \frac{G}{\rho R_0{}^2}(k+1)\left[4 + k + \frac{k(k+1)}{3}\right] + \frac{\Gamma}{\rho R_0{}^3}(k+1)(k-1)(k+2). \tag{25}$$

When f is imposed, eqn (25) defines a radius at which a given shape mode k resonates, corresponding to the minima of the coloured tongues in Fig. 6. In some particular cases (here, for k = 5 and 6), both the spherical mode and the shape mode resonate around R_{m}, resulting in particularly low critical pressures $p_{c,5}$ and $p_{c,6}$, as observed in Fig. 6 and in the experiments.

Acknowledgements

The authors wish to thank M. De Corato, J. Tsamopoulos and Y. Dimakopoulos for stimulating discussions and their critical reading of the paper. They also thank D. Baresch for his help with the design of the experimental setup. This work is supported by European Research Council Starting Grant No. 639221 (V. G.).

Notes and references

1 P. Coussot, *J. Non-Newtonian Fluid Mech.*, 2014, **211**, 31–49.
2 D. Bonn, M. M. Denn, L. Berthier, T. Divoux and S. Manneville, *Rev. Mod. Phys.*, 2017, **89**, 035005.
3 S. Stein and H. Buggisch, *J. Appl. Math. Mech.*, 2000, **80**, 827–834.
4 K. Hyun, M. Wilhelm, C. O. Klein, K. S. Cho, J. G. Nam, K. H. Ahn, S. J. Lee, R. H. Ewoldt and G. H. McKinley, *Prog. Polym. Sci.*, 2011, **36**, 1697–1753.
5 P. Lidon, L. Villa and S. Manneville, *Rheol. Acta*, 2017, **56**, 307–323.
6 J. Goyon, A. Colin, G. Ovarlez, A. Ajdari and L. Bocquet, *Nature*, 2008, **454**, 84.
7 A. Nicolas, E. E. Ferrero, K. Martens and J.-L. Barrat, *Rev. Mod. Phys.*, 2018, **90**, 045006.
8 C. J. Dimitriou and G. H. McKinley, *J. Non-Newtonian Fluid Mech.*, 2019, **265**, 116–132.
9 Y. Dimakopoulos, M. Pavlidis and J. Tsamopoulos, *J. Non-Newtonian Fluid Mech.*, 2013, **200**, 34–51.
10 A. D. Mazzeo, M. E. Lustrino and D. E. Hardt, *Polym. Eng. Sci.*, 2012, **52**, 80–90.
11 J. A. Koch, D. I. Castaneda, R. H. Ewoldt and D. A. Lange, *Cem. Concr. Res.*, 2019, **115**, 31–42.
12 M. S. Plesset and A. Prosperetti, *Annu. Rev. Fluid Mech.*, 1977, **9**, 145–185.
13 B. Dollet, P. Marmottant and V. Garbin, *Annu. Rev. Fluid Mech.*, 2019, **51**, 331–355.
14 C. C. Coussios and R. A. Roy, *Annu. Rev. Fluid Mech.*, 2008, **40**, 395–420.
15 C. W. Barney, C. E. Dougan, K. R. McLeod, A. Kazemi-Moridani, Y. Zheng, S. Ye, Z. Tiwari, I. Sacligil, R. A. Riggleman, S. Cai, J.-H. Lee, S. R. Peyton, G. N. Tew and A. J. Crosby, *Proc. Natl. Acad. Sci. U. S. A.*, 2020, **117**, 9157–9165.
16 A. Jamburidze, M. De Corato, A. Huerre, A. Pommella and V. Garbin, *Soft Matter*, 2017, **13**, 3946–3953.
17 J. B. Estrada, C. Barajas, D. L. Henann, E. Johnsen and C. Franck, *J. Mech. Phys. Solids*, 2018, **112**, 291–317.
18 Y. Holenberg, O. M. Lavrenteva, A. Liberzon, U. Shavit and A. Nir, *J. Non-Newtonian Fluid Mech.*, 2013, **193**, 129–143.
19 G. Karapetsas, D. Photeinos, Y. Dimakopoulos and J. Tsamopoulos, *J. Fluid Mech.*, 2019, **865**, 381–413.
20 M. De Corato, B. Saint-Michel, G. Makrigiorgos, Y. Dimakopoulos, J. Tsamopoulos and V. Garbin, *Phys. Rev. Fluids*, 2019, **4**, 073301.
21 P. Saramito, *J. Non-Newtonian Fluid Mech.*, 2009, **158**, 154–161.
22 S. Iwata, Y. Yamada, T. Takashima and H. Mori, *J. Non-Newtonian Fluid Mech.*, 2008, **151**, 30–37.
23 A. Prosperetti, *Phys. Fluids*, 1982, **25**, 409–410.
24 A. Prosperetti, *J. Acoust. Soc. Am.*, 1977, **61**, 17–27.
25 S. M. van der Meer, B. Dollet, M. M. Voormolen, C. T. Chin, A. Bouakaz, N. de Jong, M. Versluis and D. Lohse, *J. Acoust. Soc. Am.*, 2007, **121**, 648–656.
26 F. Hamaguchi and K. Ando, *Phys. Fluids*, 2015, **27**, 113103.
27 M. Minnaert, *London, Edinburgh Dublin Philos. Mag. J. Sci.*, 1933, **16**, 235–248.
28 L. A. Crum, *J. Acoust. Soc. Am.*, 1975, **57**, 1363–1370.
29 T. G. Leighton, A. J. Walton and M. J. W. Pickworth, *Eur. J. Phys.*, 1990, **11**, 47.
30 Y. A. Ilinskii, G. D. Meegan, E. A. Zabolotskaya and S. Y. Emelianov, *J. Acoust. Soc. Am.*, 2005, **117**, 2338–2346.
31 M. W. Urban, I. Z. Nenadic, S. A. Mitchell, S. Chen and J. F. Greenleaf, *J. Acoust. Soc. Am.*, 2011, **130**, 1133–1141.
32 C. W. Macosko, *Rheology: Principles, Measurements and Applications*, Wiley-VCH, New York, 1994.
33 R. Hill, *The mathematical theory of plasticity*, Oxford University Press, 1998, vol. 11.
34 D. Sikorski, H. Tabuteau and J. R. de Bruyn, *J. Non-Newtonian Fluid Mech.*, 2009, **159**, 10–16.
35 J.-M. Piau, *J. Non-Newtonian Fluid Mech.*, 2007, **144**, 1–29.
36 P. Lefrançois, E. Ibarboure, B. Payré, E. Gontier, J.-F. L. Meins and C. Schatz, *J. Appl. Polym. Sci.*, 2015, **132**, 42761.
37 M. Dinkgreve, M. Fazilati, M. Denn and D. Bonn, *J. Rheol.*, 2018, **62**, 773–780.
38 L. Jørgensen, M. Le Merrer, H. Delanoë-Ayari and C. Barentin, *Soft Matter*, 2015, **11**, 5111–5121.
39 *CRC Handbook of Chemistry and Physics*, ed. J. Rumble, CRC Press, 2019.
40 P. M. Morse and R. H. Bolt, *Rev. Mod. Phys.*, 1944, **16**, 69.
41 M. Guédra, S. Cleve, C. Mauger, P. Blanc-Benon and C. Inserra, *Phys. Rev. E*, 2017, **96**, 063104.
42 M. Versluis, D. E. Goertz, P. Palanchon, I. L. Heitman, S. M. van der Meer, B. Dollet, N. de Jong and D. Lohse, *Phys. Rev. E*, 2010, **82**, 026321.
43 V. Poulichet, A. Huerre and V. Garbin, *Soft Matter*, 2017, **13**, 125–133.
44 K. Murakami, R. Gaudron and E. Johnsen, *Ultrason. Sonochem.*, 2020, **67**, 105170.
45 A. O. Maksimov and T. G. Leighton, *Acta Acust. Acust.*, 2001, **87**, 322–332.
46 F. Mekki-Berrada, P. Thibault and P. Marmottant, *Phys. Fluids*, 2016, **28**, 032004.
47 S. Cleve, M. Guédra, C. Mauger, C. Inserra and P. Blanc-Benon, *J. Fluid Mech.*, 2019, **875**, 597–621.
48 K. Foteinopoulou and M. Laso, *Ultrasonics*, 2010, **50**, 758–776.
49 A. A. Doinikov, *J. Fluid Mech.*, 2004, **501**, 1–24.
50 A. Jaishankar and G. H. McKinley, *Proc. – R. Soc. Edinburgh, Sect. A: Math.*, 2013, **469**, 20120284.
51 T. G. Mason, *Rheol. Acta*, 2000, **39**, 371–378.
52 M. Caggioni, V. Trappe and P. T. Spicer, *J. Rheol.*, 2020, **64**, 413–422.
53 P. Lidon, L. Villa and S. Manneville, *Soft Matter*, 2019, **15**, 2688–2702.
54 J. Happel and H. Brenner, *Low Reynolds number hydrodynamics*, Springer, 1983, DOI: 10.1007/978-94-009-8352-6.
55 K. Niedzwiedz, H. Buggisch and N. Willenbacher, *Rheol. Acta*, 2010, **49**, 1103–1116.
56 X. Zhang, O. Fadoul, E. Lorenceau and P. Coussot, *Phys. Rev. Lett.*, 2018, **120**, 048001.
57 S. Varchanis, S. J. Haward, C. C. Hopkins, A. Syrakos, A. Q. Shen, Y. Dimakopoulos and J. Tsamopoulos, *Proc. Natl. Acad. Sci. U. S. A.*, 2020, **117**, 12611–12617.

58 J. Song, M. Caggioni, T. M. Squires, J. F. Gilchrist, S. W. Prescott and P. T. Spicer, *Rheol. Acta*, 2019, **58**, 217–229; J. Song, M. Caggioni, T. M. Squires, J. F. Gilchrist, S. W. Prescott and P. T. Spicer, *Rheol. Acta*, 2019, **58**, 231–239.
59 D. E. V. Andrade and P. Coussot, *Soft Matter*, 2019, **15**, 8766–8777.
60 S. Saha, B. Saint-Michel, V. Leynes, B. P. Binks and V. Garbin, *Rheol. Acta*, 2020, **59**, 255–266.